



Pinning effect of spheroid second-phase particles on grain growth studied by three-dimensional phase-field simulations

Liesbeth Vanherpe^{a,*}, Nele Moelans^b, Bart Blanpain^b, Stefan Vandewalle^a

^a Department of Computer Science, Katholieke Universiteit Leuven, Celestijnenlaan 200A, B-3001 Leuven, Belgium

^b Department of Metallurgy and Materials Engineering, Katholieke Universiteit Leuven, Kasteelpark 44, B-3001 Leuven, Belgium

ARTICLE INFO

Article history:

Received 4 March 2010

Received in revised form 30 April 2010

Accepted 7 May 2010

Keywords:

Grain growth

Zener pinning

Phase-field modelling

Microstructure

Numerical simulation

ABSTRACT

For the first time, the pinning effect of small spheroid particles with aspect ratios 1, 2 and 3 on grain growth in polycrystalline structures was studied by three-dimensional phase-field simulations. This was possible by using an efficient parallel sparse bounding box algorithm. Simulation results for different volume fractions of the second-phase particles show that distributions of particles with higher aspect ratios have a stronger pinning effect, since grain boundaries have the tendency to align with the largest cross-section of the particles. The number of particles at triple, quadruple or higher order junctions increases with volume fraction, and with aspect ratio. Nevertheless, the final grain size has a volume fraction dependence of the form $1/f_v^{0.93}$, following theoretical predictions assuming random intersections between grain boundaries and particles. A generalised Zener relation with a prefactor depending on the aspect ratio is proposed.

© 2010 Elsevier B.V. All rights reserved.

1. Introduction

The microstructure of materials is often composed of multiple grains with different crystallographic orientations. Under certain conditions, the larger grains will start to grow and the smaller grains will shrink. This phenomenon, called grain growth, is thus characterised by an increase of the mean grain size. Small second-phase particles, such as precipitates and insoluble inclusions, exert a strong pinning effect, also called Zener pinning, on the grain boundaries. They restrain the mobility of grain boundaries and eventually inhibit grain growth, limiting the final mean grain size of the microstructure. Insight into the pinning effect of particles is of great technological importance, since for many applications a tailored grain size is required to obtain materials with the desired properties. Examples are the addition of a small amount of alloying elements to High Strength Low Alloyed (HSLA) steels and Ni-based super alloys in order to obtain materials with a small grain size and high strength [1–3], the use of precipitates in thin films to induce abnormal grain growth in order to obtain films with a large grain size for high electrical conductivity and reduced electromigration damage [4–6], and, recently also the use of particles (such as precipitates, carbon nanotubes and organic or amorphous particles) to stabilize nanocrystalline materials [7–10].

In most analytical studies [11–14] on Zener pinning it is assumed that normal grain growth is arrested when a critical mean grain radius $\langle R \rangle_{\text{lim}}$ is reached. Most often a relation of the form

$$\frac{\langle R \rangle_{\text{lim}}}{r} = K \frac{1}{f_v^b} \quad (1)$$

is obtained, where r is the radius of the second-phase particles and f_v the volume fraction. The values of the parameters K and b vary among the different studies, depending on which assumptions are made on the shape and properties of the particles and boundaries, and on the assumptions made on the position of the particles with respect to the boundaries.

The pinning force exerted by one particle on a grain boundary can be analytically calculated based on the position of the boundary, the shape of the particle and the properties of the particle–matrix interface and grain boundary [11,14–16]. The calculation of the total pinning force of a distribution of multiple particles is more complex. The number of particles that lie at a grain boundary, as well as the geometry of the grain boundary at and near each grain boundary–particle intersection, has to be known. However, this appears to be extremely difficult to describe analytically. In this respect, computer simulations turn out to be helpful. They are a practical tool, not only to determine the number and the geometry of boundary–particle intersections, but also to study the role of different characteristics of the second-phase particles separately. Together with existing analytical theories and experimental findings, they provide valuable insights.

* Corresponding author. Tel.: +32 16 327663; fax: +32 16 327996.

E-mail address: liesbeth.vanherpe@cs.kuleuven.be (L. Vanherpe).

The pinning effect of second-phase particles has mostly been studied by two-dimensional computer simulations using Monte Carlo Potts models [17–19], front-tracking-type models [20–22] and phase-field models [23–30]. It is found that for two-dimensional systems, relation (1) is obeyed, with $b = 0.5$, and most particles are in contact with a grain boundary in the pinned microstructure. Only few studies consider three-dimensional systems. Simulations for three-dimensional systems [19,26,27] show that the fraction of particles in contact with a grain boundary is significantly lower than in two-dimensional systems. Furthermore, fitting of relation (1) to the results obtained from three-dimensional simulations gives values for b and K that are very different from those obtained for two-dimensional simulations. In [19], $b = 1.02$ and $K = 0.728$ are obtained; in [22], the value $b = 1.0$ is extracted. In contrast, in the work of [26], the parameter values $b = 0.870$ and $K = 1.42$ are found. The study in [27] shows that even for columnar grain structures, the pinning effect is very different from that observed in two-dimensional simulations. In two dimensions, the grain boundaries are basically lines interacting with particles, which split into two different boundary segments when they meet a particle. In contrast, in three dimensions, the grain boundaries are surfaces that remain a single entity when meeting a particle. In order to balance the interfacial tensions at a particle-boundary intersection, the grain boundary assumes a so-called dimple shape. The extra curvature thus created contributes to the driving force of grain growth [31]. Furthermore, in two dimensions, the pinning force of one particle is maximal when the grain boundary meets the particle at an angle which is twice as large as is the case in three dimensions. Therefore, the pinning effect in two-dimensional systems is in general much stronger than in three-dimensional systems [27]. It is thus important that predictive computer models reflect the three-dimensional nature of Zener pinning for bulk material systems as well as for thin films.

Although the values obtained for the coefficients in the Zener relation in the different simulation studies seem to vary considerably, it was shown in [26,28] that the limiting mean grain sizes obtained with different simulation techniques, in fact, agree quite well. Experimentally determined limiting mean grain sizes are however in general much smaller than those predicted by simulations. Based on experimental data, it was also concluded that the Zener relation should have different parameter values for respectively low and high volume fractions [13,14]. Such a transition between two regimes has not been observed in computer simulations. These discrepancies between experimental and theoretical results indicate that one or several essential aspects were not considered in previous computer simulations. A possible hypothesis is the effect of particle shape. Except for [29], all the above mentioned studies only performed simulations of grain growth in the presence of spherical particles. In reality, however, particles are generally not spherical. Experimental microstructures show that, even in the case where the particle–matrix interface is incoherent and has properties that are independent of orientation, the particle shape deviates from spherical because of inhomogeneities in the surrounding matrix during formation of the particle [32]. For example, particles formed on a former boundary are lance-shaped, the solute flux for particles formed near another particle or a grain boundary is not spherically symmetric, particles may change shape in an anisotropic way during deformation processes. It has been shown that the pinning force of a single particle is strongly dependent on the geometry at the grain boundary–particle sections and the particle shape [11,15,19,33]. The effect of particle shape seems to be even far more important than the effect of the anisotropy of the particle–matrix interfacial energy [11,15]. The advantage of phase-field simulations is that simulations can be performed and the effect of particle dispersions can be computed

without making prior assumptions on the number of particles interacting with the grain boundaries and their orientations with respect to the boundary.

According to [34], the maximal pinning force F_Z of an ellipsoid particle is, for the case where the boundary intersects the particle perpendicular to its major axis,

$$F_Z = F_Z^S \frac{2}{(1 + r_a)r_a^{1/3}} \quad (2)$$

and, for the case where the boundary intersects the particle along a plane containing the major axis,

$$F_Z = \frac{F_Z^S}{\pi} \frac{(1 + 2.14 r_a)}{r_a^{1/3}}, \quad r_a \geq 1, \quad (3)$$

where r_a is the aspect ratio of the particle and F_Z^S the drag from a spherical particle of equal volume. The last equation shows that if the boundary intersects the particle along a plane containing the major axis, its pinning force is considerably larger than that of a spherical particle with equal volume, even for small aspect ratios. If the boundary intersects the particle perpendicular to the major axis, the pinning force of the particle is however much smaller than that of a spherical particle. As a consequence, the effect of particle shape on the overall pinning effect of a particle distribution depends on the possibility that the boundary–particle intersection contains the major axis. In [15], it was analytically calculated that within well-defined conditions, particle dispersions of mono-orientation can be very effective in pinning migrating boundaries. This was confirmed by the results of two-dimensional phase-field simulations in [29], which show that a dispersion of mono-oriented ellipse-shaped particles with a high aspect ratio is more effective in pinning than a dispersion of circular particles of the same size.

Based on the work of [15,34], it is generally assumed that dispersions of ellipsoid particles have a stronger pinning effect than dispersion of spherical particles, although to our knowledge, the effect of random dispersions of ellipsoid particles on grain growth has not been verified by three-dimensional mesoscale simulations yet, mainly because of computational limitations. To gain more insight in the dependence of the pinning force of a particle distribution on the shape of the particles, we performed three-dimensional phase-field simulations of grain growth in systems with spheroid particles for different aspect ratios and volume fractions of the particles. Phase-field modelling is a versatile tool for simulating microstructural evolution phenomena. It allows one to predict the evolution of complex morphologies with different thermodynamic driving forces. In [35], a phase-field model is used to model the microstructure of a single-phase material by a set of non-conserved phase-field variables that distinguish the different crystallographic orientations of the grains. Inside a grain, one phase-field variable takes the non-zero equilibrium value 1, while the other variables assume values close to zero. Across the grain boundaries, the corresponding phase-field variables vary continuously to their equilibrium value in the neighbouring grains. In this work, we employ an extension of this model for grain growth in the presence of incoherent second-phase particles with constant properties presented in [24,25,27]. The effect of aspect ratio and volume fraction was studied for incoherent spheroid particles with aspect ratios 1, 2 and 3. A parallelised bounding box algorithm [28] is applied to make three-dimensional simulations with a large amount of grains feasible. The purpose of this work is to provide new information that might lead to a generalisation of the classical Zener type pinning theories to the effect of spheroid particles on grain growth.

2. Phase-field model and discretisation

2.1. Phase-field model

In accordance with [35], the employed phase-field model represents the microstructure of a single-phase polycrystalline material by a set of p phase-field variables

$$\eta_1(\mathbf{r}, t), \eta_2(\mathbf{r}, t), \dots, \eta_p(\mathbf{r}, t). \quad (4)$$

The phase-field variables distinguish the different crystallographic orientations of the grains present in the microstructure. They are continuous functions of the spatial coordinates and time. The spatial and temporal evolution of the phase-field variables is governed by the time-dependent Ginzburg–Landau equations

$$\frac{\partial \eta_i(\mathbf{r}, t)}{\partial t} = -L \frac{\delta F}{\delta \eta_i(\mathbf{r}, t)}, \quad i = 1, \dots, p, \quad (5)$$

where the kinetic coefficient L is related to the grain boundary mobility. The free energy F of the system is described by

$$F = \int_V \left(\sum_{i=1}^p \left(\frac{\eta_i^4}{4} - \frac{\eta_i^2}{2} \right) + \sum_{i=1}^p \sum_{j \neq i}^p \eta_i^2 \eta_j^2 + \frac{\kappa}{2} \sum_{i=1}^p (\nabla \eta_i)^2 \right) d^3 \mathbf{r}, \quad (6)$$

with κ the gradient energy coefficient. In this work, isotropic grain boundary energy and mobility are assumed and thus the coefficients κ and L are constants. Grain boundary energy and width scale with $\sqrt{\kappa}$ [36].

In [24,25], this phase-field model is extended for simulating grain growth in materials containing small incoherent second-phase particles with constant properties. To include such particles in the model, a spatially dependent parameter ϕ is added. This parameter ϕ equals 1 inside a particle and 0 elsewhere and remains constant in time. The free energy F of the system is now described by

$$F = \int_V \left(\sum_{i=1}^p \left(\frac{\eta_i^4}{4} - \frac{\eta_i^2}{2} \right) + \sum_{i=1}^p \sum_{j \neq i}^p \eta_i^2 \eta_j^2 + \phi^2 \sum_{i=1}^p \eta_i^2 + \frac{\kappa}{2} \sum_{i=1}^p (\nabla \eta_i)^2 \right) d^3 \mathbf{r}. \quad (7)$$

Substituting (7) into (5) results in a set of reaction–diffusion partial differential equations

$$\frac{\partial \eta_i}{\partial t} = L \left(\kappa \nabla^2 \eta_i - \eta_i^3 + \eta_i - 2\eta_i \left(\sum_{j \neq i}^p \eta_j^2 + \phi^2 \right) \right), \quad i = 1, \dots, p. \quad (8)$$

Periodic boundary conditions are applied.

2.2. Particle size and shape

To study the effect of particle shape on Zener pinning, spheroid particles are added to the microstructure. The spheroid particles are characterised by their aspect ratio r_a , which is the ratio r_a between the long axis radius l and the short axis radius s . The volume V_s of a spheroid is given by

$$V_s = \frac{4}{3} \pi l s^2. \quad (9)$$

In the simulations, three different aspect ratios are applied: $r_a = 1$, $r_a = 2$, and $r_a = 3$, and the volume of the three types of spheroid particles is intended to be approximately the same. Using formula (9) in combination with the constraint that $l \geq s \geq 3$ grid points (g.p.) because of the finite width of the boundaries in the simulations [27], this gives spheroids with $l = s = 4.3$ g.p. for $r_a = 1$, $l = 6.8$ g.p. and $s = 3.4$ g.p. for $r_a = 2$, and $l = 9$ g.p. and $s = 3$ g.p. for $r_a = 3$. Fig. 1 illustrates the particle shapes after discretisation. The radii of the discretised shapes are $l = s = 4$ g.p., $l = 7$ g.p. and $s = 3$ g.p., and $l = 9$ g.p. and $s = 3$ g.p. respectively. The volume

of the spheroid particles with $r_a = 3$ ends up to be slightly larger than the volume of the other two particle types. The volume fraction of the second-phase particles f_v is defined as the number of grid points representing the second-phase particles, divided by the total number of grid points in the system. In this work, a particle is allowed to be oriented with its long axis either along the x -, the y -, or the z -axis of the system. The orientations of the particles within the same microstructure are approximately equally distributed over the three possible axes. If the particles were allowed to be oriented along every possible direction, they would differ in volume due to discretisation effects. We presume that the orientation distribution along the three axes is a reasonable approximation to a uniform orientation distribution.

2.3. Model parameters

Simulations are performed with different volume fractions $f_v = 5\%$, 6% , 8% , 10% , 11% , and 12% . For every parameter combination of aspect ratio and volume fraction, three simulation runs are executed over which all studied characteristics are averaged. The initial grain structure and particle distribution is entirely different for every simulation run. There is however a correspondence between the simulation runs for the same aspect ratio or equal volume fraction: the particles are located at similar locations, which allows one to compare the resulting microstructures visually. Since particle clusters also occur in real materials, no effort was made to separate the second-phase particles: some particles may therefore overlap. As in [37], we assume that the influence of this small amount of particle clusters on the pinning effect is small.

All simulations evolve on a $256 \times 256 \times 256$ grid, with $p = 25,000$, $\Delta t = 0.2$, and $\Delta x = 1$. After 1000 time steps, about 1000 of the 25,000 possible orientations remain. To visualize the simulation results, a diffuse interface representation is used, and the sum $\sum_{i=1}^p \eta_i^2(\mathbf{r})$ is displayed. Since we are mostly interested in the final grain size where grain growth is arrested, which is independent of the grain boundary energy and mobility (see relation (1)), the exact value of the model parameters L and κ is not important. Therefore, we take similar values as in previous studies [27,28], namely $\kappa = 0.5$ and $L = 1$. The choice of these parameters values is justified in [25].

2.4. Discretisation

Model Eq. (8) are solved by using a finite difference scheme. The spatial derivative is discretised with second order central differences. For $\mathbf{r} = (x, y, z)$, we have

$$\nabla^2 \eta_i(\mathbf{r}) = \sum_{v=x,y,z} \frac{\eta_i(v + \Delta v) - 2\eta_i(v) + \eta_i(v - \Delta v)}{(\Delta v)^2}, \quad (10)$$

where Δx , Δy and Δz denote the mesh widths in the finite difference grid. The time derivative is discretised using a first order semi-implicit scheme [38]. The diffusion part is treated implicitly, the reaction part explicitly:

$$\frac{\eta_i^{n+1} - \eta_i^n}{\Delta t} = L \left[\left(\kappa \nabla^2 \eta_i \right)^{n+1} + \left(-\eta_i^3 + \eta_i - 2\eta_i \left(\sum_{j \neq i}^p \eta_j^2 + \phi^2 \right) \right)^n \right], \quad i = 1, \dots, p, \quad (11)$$

where the superscript n indicates the solutions at time step n . The implicit treatment of the Laplacian, combined with the explicit treatment of the non-linear coupling of the phase-field variables, allows the use of a large time step without the need to solve one very large coupled system of equations. It effectively decouples

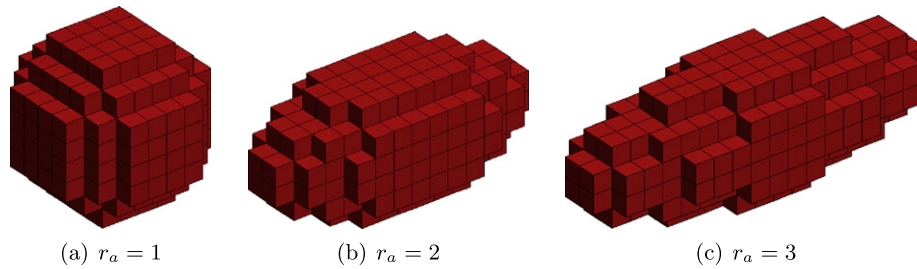


Fig. 1. Three different spheroid shapes of the second-phase particles after discretisation, with approximately equal volume. They are characterised by the ratio r_a between the length l of the long axis radius and the length s of the short axis radius.

the system into p scalar diffusion equations, to be solved at every time step.

3. Bounding box algorithm

Because three-dimensional grain growth simulations demand significant amounts of computation power, recently, several efficient sparse algorithms have been developed which exploit the observation that at a given location in a microstructure, only a few crystallographic orientations are active [28,39–42]. These sparse algorithms show significant improvements over conventional algorithms as they scale with the size of the microstructure instead of with the number of crystallographic orientations involved. In [28,42], a sparse bounding box algorithm is proposed that computes the phase-field model only within cuboid hulls of so-called grain regions. In contrast with the algorithms described above, it is appropriate for implicit and semi-implicit time stepping schemes. Moreover, its data structure has definite advantages in post-processing [28]. For this work, the initialization procedure described in [28] was adapted.

3.1. Concepts

A phase-field variable η_i is *active* at a grid point \mathbf{r} when $|\eta_i(\mathbf{r})| > \epsilon$, with ϵ a small positive value. In the interior of a grain, only one phase-field variable is active. Near grain boundaries, only the phase-field variables corresponding to the neighbouring grains are active. We define a *grain region* G_i as the set

$$G_i = \{(\mathbf{r}, \eta_i(\mathbf{r})) : |\eta_i(\mathbf{r})| > \epsilon \text{ and } \mathbf{r} \text{ are connected}\}. \quad (12)$$

To take periodic boundary conditions into account, the grain regions are allowed to wrap around the grid boundaries. Also, the grain regions can overlap, which allows them to interact. For each G_i , a bounding box is established as the smallest cuboid grid part containing its grid points \mathbf{r} . The set B_i is now defined as

$$B_i = \{(\mathbf{r}, \eta_i(\mathbf{r})) : \mathbf{r} \text{ lies inside the bounding box of } G_i\}. \quad (13)$$

3.2. Initialisation procedure

To initialise a microstructure, a set of spherical grain nuclei is spread over the domain, together with a distribution of second-phase particles. For every phase-field variable η_i , with $i = 1, \dots, p$, a grid point C_i is chosen according to a uniform distribution over the system domain. Next, a spherical grain region G_i with a small radius equal to s , the short axis radius of the second-phase particles, is created with C_i as its centre. Finally, the corresponding bounding box and the set B_i are determined. Thanks to the assignment of unique phase-field variables to every grain region,

subsequent grain growth simulations are performed in a coalescence-free way.

The second-phase particles are generated in a similar way. Until the desired volume fraction f_v of particles is obtained, new particles are added to the microstructure. For each particle, first, a grid point is chosen according to a uniform distribution over the system domain as the centre of the new particle. Second, a particle orientation is generated according to a uniform distribution over the three possible orientations (see Section 2.2). Finally, an array is constructed that contains the linearised coordinates of all grid points occupied by a second-phase particle. In this way, the parameter ϕ is implicitly represented.

3.3. Simulation

From this initial data structure, a grain growth simulation is started and microstructure evolution is computed. The spherical grains start to grow and impinge. Within each time step, the solution of the Eq. (8) is computed for every set B_i . Next, the algorithm checks whether the grain region G_i has shrunk or grown, and updates the bounding box and B_i accordingly. By restricting the calculations to the values within the bounding boxes, a considerable amount of computing time and memory is saved [28].

3.4. Parallel computing

To accelerate the simulations, the bounding box algorithm was parallelised. A number w_k of sets B_i is assigned to every involved processor P_k , with $k = 1, \dots, K$, and K the total number of processors. Within each time step, processor P_k computes the solution of Eq. (8) for the assigned subset of w_k sets. To simplify the computations, Eq. (8) can be rewritten as

$$\frac{\partial \eta_i}{\partial t} = L \left(\kappa \nabla^2 \eta_i + \eta_i^3 + \eta_i - 2\eta_i \left(\sum_{j=1}^p \eta_j^2 + \phi^2 \right) \right), \quad i = 1, \dots, p. \quad (14)$$

To solve Eq. (14), sum $\sum_{j=1}^p \eta_j^2$ has to be computed. First, every processor P_k computes the partial sum

$$S_k = \sum_{\substack{j=1 \\ j \in D_k}}^p \eta_j^2, \quad (15)$$

where D_k is the set of indices j for which η_j is included in the set B_j , belonging to processor P_k . Next, the partial sums S_k are summed over all the processors, by performing the `MPI_Allreduce`-operation. This approach to parallelisation divides the computing work and the memory over the processors, thus accelerating the simulation process and alleviating the memory requirements for the individual processors.

4. Results

4.1. Growth kinetics

Fig. 2 depicts the time evolution of the mean grain radius for different volume fractions f_v , for $r_a = 1$, $r_a = 2$, and $r_a = 3$ separately. For the three particle types, the pinning effect is stronger for larger volume fractions: grain growth is arrested earlier and the limiting grain size is smaller. This is in agreement with results from previous simulation studies for spherical particles [19,26] and experimental data.

In Fig. 3, the time evolution of the mean grain radius is shown for the different aspect ratios r_a , for each studied volume fraction f_v separately. Except for the parameter combination of $f_v = 6\%$ and $r_a = 3$, for every volume fraction, grain growth stops earlier and at a lower mean grain size for increasing aspect ratio. This result is qualitatively in agreement with the two-dimensional simulations of [29].

In one simulation run, for the parameter combination of $f_v = 5\%$ and $r_a = 1$, grain growth was not arrested by the particles and the final microstructure only contained one grain, while in another run, only nine grains were present in the microstructure at equilibrium. To preserve a smooth graph on Fig. 2a and Fig. 3a, we removed the corresponding data points. Otherwise, the graphs in question would go up, rather than stabilize at a limiting value. According to [43], abnormal grain growth is possible in the presence of a stable particle distribution for small grain sizes. Another reason, more plausible for the present case, might be the statistical nature of the results in combination with the finite dimensions and periodic boundary conditions assumed in the simulations. The latter reason also explains why in another simulation run, for the parameter combination of $f_v = 6\%$ and $r_a = 3$, grain growth stopped later than expected. This is reflected in Fig. 2c, where the graphs corresponding to $f_v = 5\%$ and 6% almost coincide. Table 1 lists the number of grains present in the microstructures when grain growth is stopped, for every parameter combination. The number of grains remaining in a microstructure is in keeping with the limiting grain size: for a smaller limiting size, the limiting number of grains is larger.

4.2. Cross-section

To gain more insight in the location of the particles in the microstructure, cross-sections through the middle of pinned structures are shown in Fig. 4 for simulations with $f_v = 5\%$ and 12% , and $r_a = 2$ and 3 . The figures illustrate that the limiting grain size is smaller for higher volume fractions and for higher aspect

ratio. Particles with $r_a = 3$ seem to make up a substantial part of the grain boundaries. At certain points in the microstructure, they have a significant influence on the grain boundary orientation: the grain boundaries follow their orientation in such a way that the particles constitute a part of the boundaries. In this way, the particles are more efficient in pinning grain boundaries compared to the particles with aspect ratio $r_a = 2$. The extra amount of grain boundary that has to be created for this reorientation appears to outweigh the amount of grain boundary that is removed by the particles with r_a smaller than 3.

4.3. Particle location

At equilibrium, many of the second-phase particles are located at grain boundaries. According to their location, the particles that intersect with grain boundaries can be subdivided into four types: the particles present at faces between two grains, at places where three grains meet, at places where four grains meet and at junctions where more than four grains meet. Fig. 5 reflects the fraction ϕ_{tot} of particles present at grain boundaries, subdivided according to their particular locations, for the three aspect ratios r_a separately. In agreement with previous studies for spherical particles, the graphs show that the total fraction of particles present at boundaries increases with f_v . The present study shows furthermore that this increase of the fraction of particles in contact with a boundary with f_v is mainly due to an increase of the number of particles located at triple and quadruple junctions, while the fraction of particles located at grain faces is more or less independent of the volume fraction of the particles for $r_a = 1$ and slightly decreases for higher aspect ratios. The amount of particles located at junctions of more than four grains, slightly increases for aspect ratio $r_a = 1$, while for aspect ratio $r_a = 3$, the fraction ϕ_n of particles present at junctions where more than four grains meet, is considerable at higher volume fractions. The tendency of the particles to lie at multiple junctions at higher volume fractions is thus stronger for higher aspect ratio.

In Fig. 6, the fractions ϕ_i are shown as a function of r_a , for different volume fractions separately. This representation clearly shows that, except for statistical variations, the pinning behaviour changes with aspect ratio: for higher aspect ratio, particles lie on multiple junctions rather than at grain boundary faces. This tendency becomes much more pronounced for larger volume fractions, as the amount of particles at multiple junctions relative to ϕ_{tot} increases and the grain size compared to the particle size decreases with volume fraction. Particles with $r_a = 3$ thus have a significant influence on the microstructure topology, especially at high volume fractions. We expect that the effect of particle shape

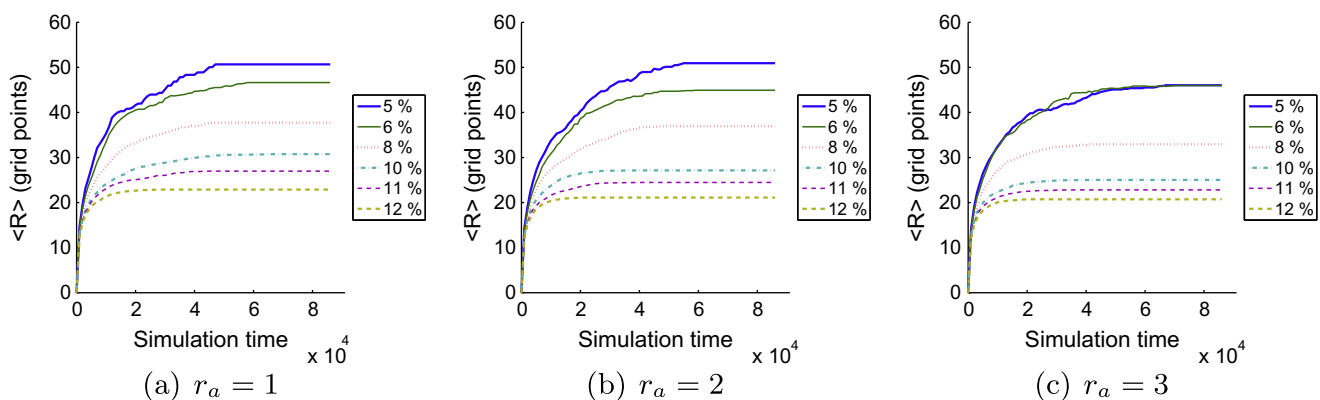


Fig. 2. Time evolution of the mean grain radius $\langle R \rangle$ for different volume fractions f_v , for each studied aspect ratio r_a separately.

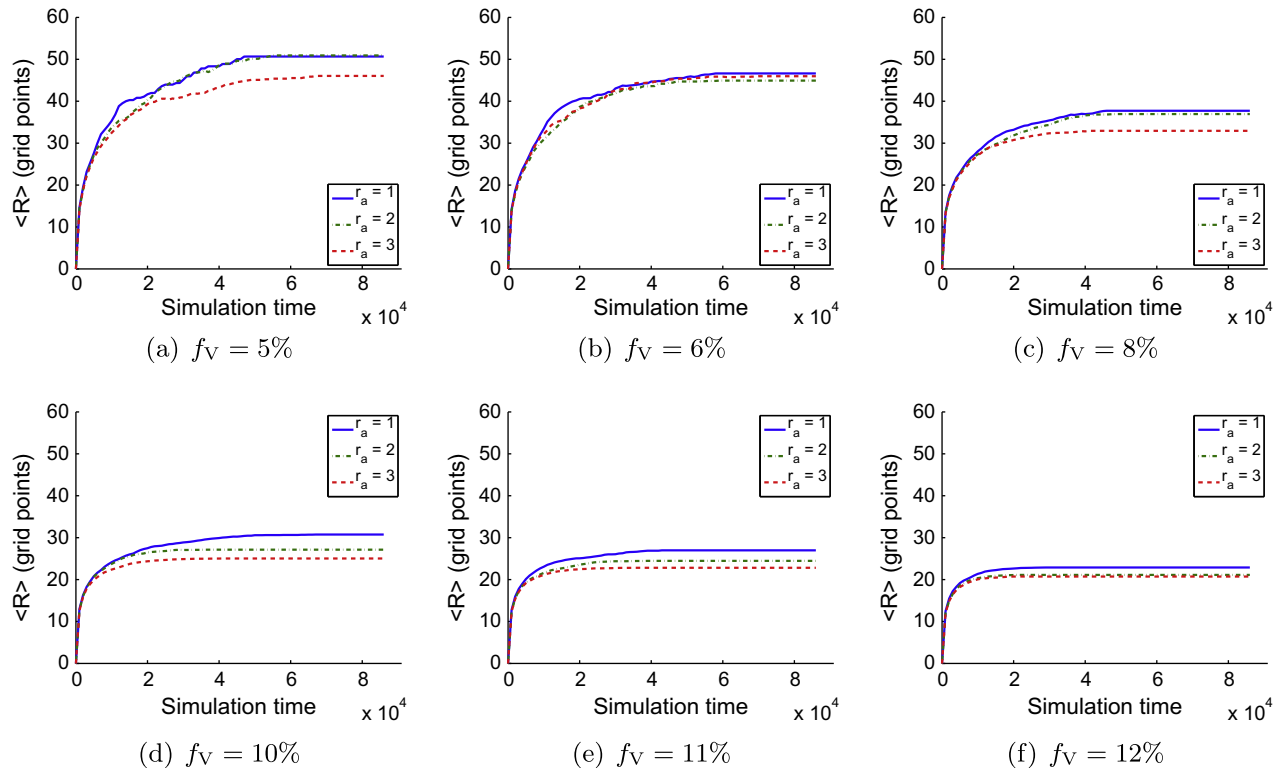


Fig. 3. Time evolution of the mean grain radius $\langle R \rangle$ for different aspect ratios r_a , for each studied volume fraction f_v separately.

Table 1

Number of grains present in the microstructures when grain growth is stopped, for every tested parameter combination. Note that the limiting number of grains for the parameter combination $f_v = 5\%$, $r_a = 1$ originates from only one simulation run, instead of three for the other parameter combinations.

	$f_v = 5\%$	$f_v = 6\%$	$f_v = 8\%$	$f_v = 10\%$	$f_v = 11\%$	$f_v = 12\%$
$r_a = 1$	27	30	62	110	170	250
$r_a = 2$	30	41	65	159	212	313
$r_a = 3$	36	38	95	198	255	330

increases further with the aspect ratio of the particles for r_a greater than 3.

4.4. Comparison with other studies

Fig. 7 shows an overview of data obtained in different studies. Our results for $\frac{\langle R \rangle_{\text{lim}}}{m} = (ls^2)^{\frac{1}{3}}$ and for aspect ratios $r_a = 1$ and $r_a = 3$ are compared with the original Zener relation $\frac{\langle R \rangle_{\text{lim}}}{r} = \frac{4}{3} \frac{1}{f_v}$ [44], the relation derived by Hillert for low ($f_v < 10\%$) and high ($f_v > 10\%$) volume fractions [13], the relation of Manohar which is based on a large compilation of experimental data [14], experimental results (not included in the data set used in [14]) for cementite particles in a ferrite matrix [45,46], and results obtained from simulations with a Monte Carlo Potts model [19] and with a phase-field model [26]. The cementite particles were characterised as ‘spherical’, but the microscopic pictures in [45] show that they have a rather irregular shape. These extra experimental data show that there is generally a large scatter on experimentally measured limiting grain sizes, even when they are obtained for the same material. Nevertheless, all experimental data points are considerably below the curves obtained for spherical particles. Our data points for the $r_a = 1$ distribution almost coincide with the relation obtained from Monte Carlo Potts simulation and are located slightly below the relation obtained from previous phase-field simulations. The simulation data points for $r_a = 3$ lie lower and thus

closer to the experimental data. If particles have a slightly irregular shape, grain boundaries have probably the tendency to align themselves with the largest cross-section of the particles.

The simulation results show that the dispersions of spheroid particles have a stronger pinning effect than the dispersions of spherical particles. The effect is however too small to fully explain the large difference between the final grain sizes obtained in simulations and those obtained experimentally.

5. Generalised Zener relation

5.1. Analysis of the simulation results

The presence of second-phase particles inhibits grain growth in such a way that grain growth stops when a limiting mean grain radius $\langle R \rangle_{\text{lim}}$ is obtained. Most theories predict a relation between $\langle R \rangle_{\text{lim}}$ and the size and volume fraction of the particles of the form (1), which is a generalisation of the Zener relation [14,44]. In the classical Zener–Smith analysis, it is assumed that particles are spherical, incoherent and that particles and boundaries intersect on a random basis. As long as the number of particles at grain boundaries is much larger than the number of particles at multiple junctions, this approximation is likely to be valid [43]. According to [14,43,45] most particles may be situated in grain corners for high volume fractions. In this case, the Zener assumptions are not applicable anymore. Nevertheless, it is seen that a Zener type relation is still appropriate at higher volume fractions, although sometimes a weaker volume fraction dependence ($b \approx 0.33$ instead of $b \approx 1$ in formula (1)) of the limiting grain size is found [14,45]. According to [45], this change in volume fraction dependence is at $f_v = 10\%$; according to [14], it is at $f_v = 5\%$.

In [15], the pinning pressure is derived for a distribution of mono-oriented spheroid particles, following the classical Zener approach. Because of the assumptions made in this approach, the

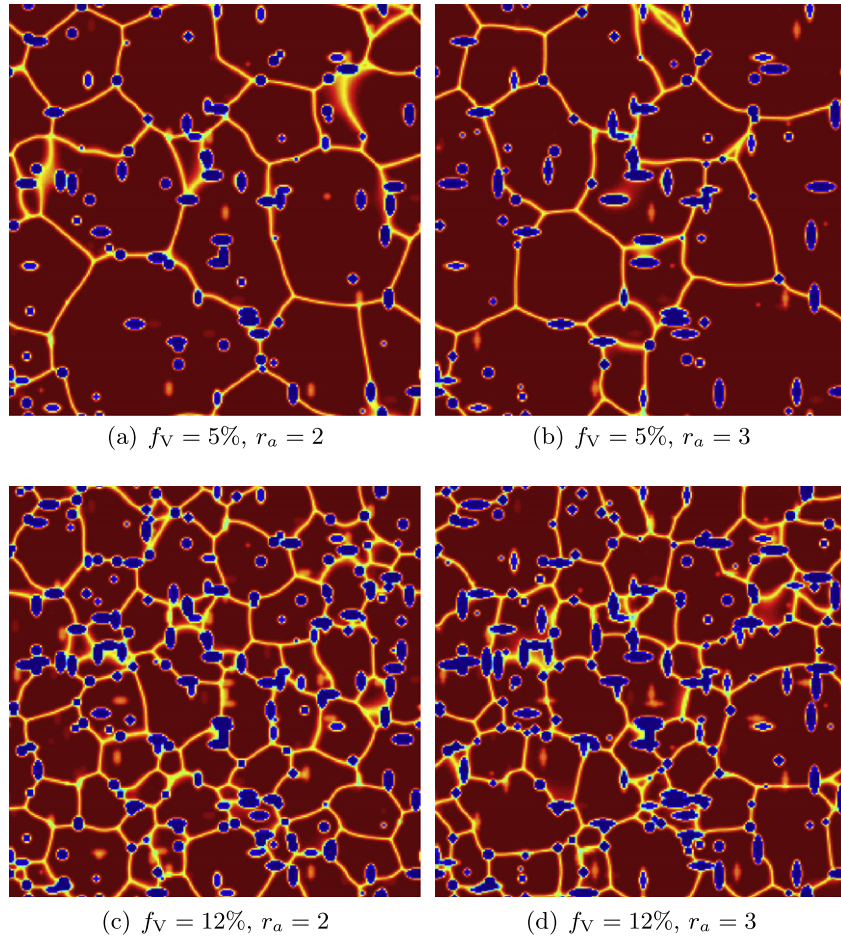


Fig. 4. Cross-sections of three-dimensional pinned structures obtained from simulations for $f_V = 5\%$ and 12% , and $r_a = 2$ and 3 . No further evolution was observed after about (a) 70,000, (b) 94,000, (c) 34,000 and (d) 34,000 time steps.

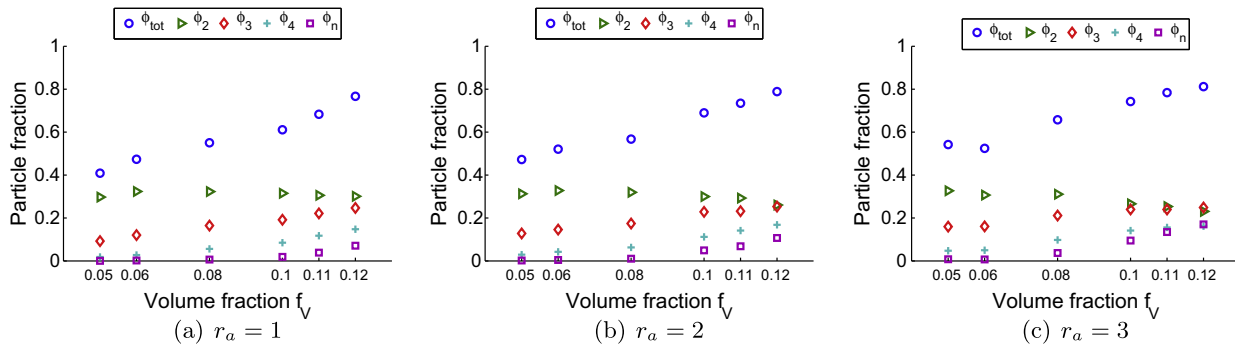


Fig. 5. Fraction ϕ_{tot} of particles located at grain boundaries, divided into four types: located at grain faces (ϕ_2), at junctions where three grains meet (ϕ_3), where four grains meet (ϕ_4), and where more than four grains meet (ϕ_n), for different aspect ratios r_a .

large differences in pinning forces for different shapes and orientations of single particles are not reflected in the computed effect of the corresponding particle distributions. It is not yet understood whether their approximations or the Zener approximations in general are applicable for spheroid particles with aspect ratio different from 1. The calculation of the total pinning effect of multiple spheroid particles proves to be a complex problem. Analysis of our simulation results can shed new light on the relation between $\langle R \rangle_{\text{lim}}$ on the one hand, and the volume fraction and the aspect ratio of the particles on the other hand.

The Zener relation (1) is formulated assuming spherical particles and their size is quantified by means of the particle radius r .

To extend the Zener relation to spheroid particles, we propose three different measures m to replace the parameter r , namely the long axis radius $m = l$, the short axis radius $m = s$, and the geometric mean $m = (ls^2)^{1/3}$ of the three axis radii, yielding a relation of the form

$$\frac{\langle R \rangle_{\text{lim}}}{m} = K \frac{1}{f_V^b}. \quad (16)$$

The last measure is often used in experimental studies to characterise the size of the particles.

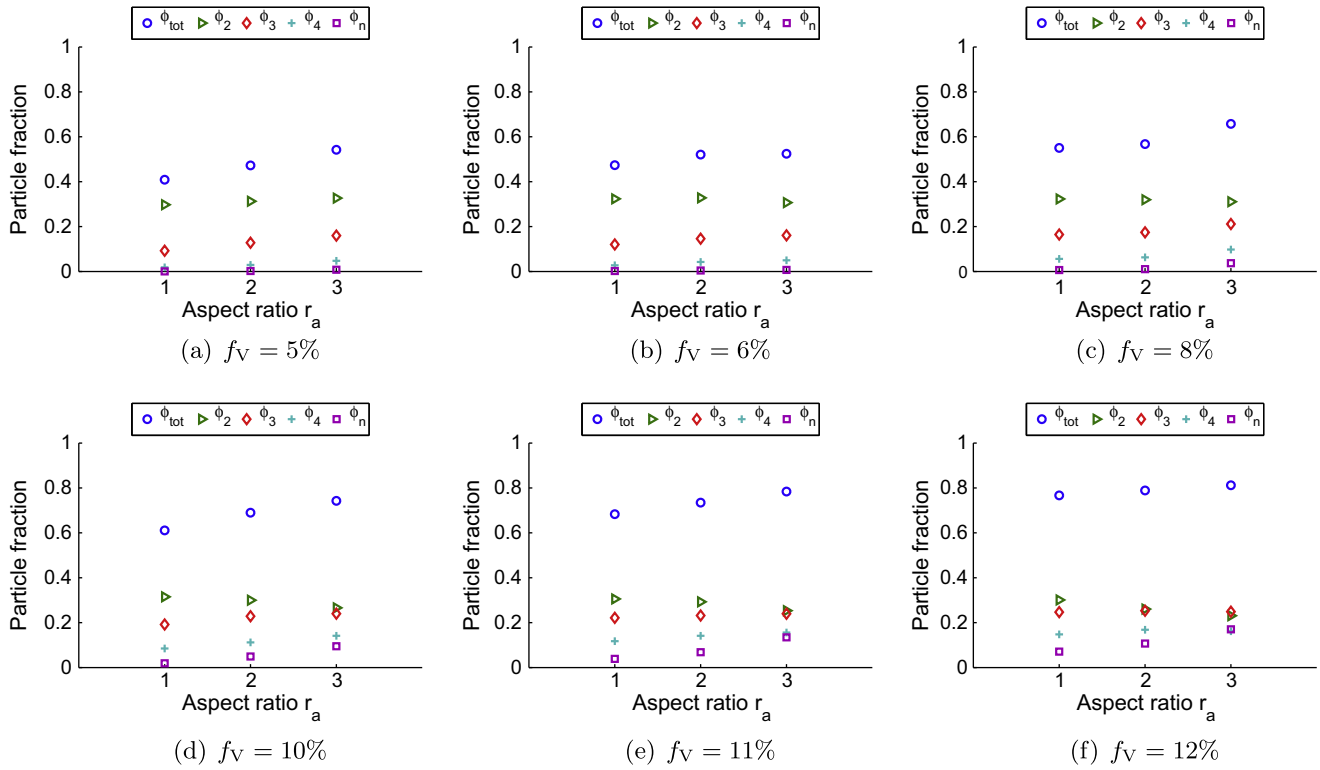


Fig. 6. Fraction ϕ_{tot} of particles located at grain boundaries, divided into four types: located at grain faces (ϕ_2), at junctions where three grains meet (ϕ_3), where four grains meet (ϕ_4), and where more than four grains meet (ϕ_n), for different volume fractions f_V .

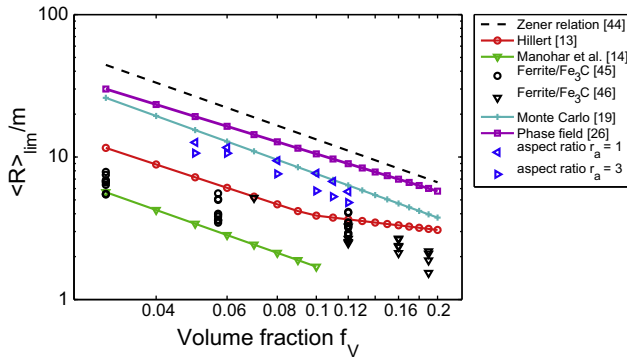


Fig. 7. Comparison of the simulation results for aspect ratios $r_a = 1$ and $r_a = 3$, for $\langle R \rangle_{\text{lim}} = (ls^2)^{\frac{1}{3}}$, with the original Zener relation [44], the relation derived by Hillert for low ($f_V < 10\%$) and high ($f_V > 10\%$) volume fractions [13], the relation of Manohar based on a large compilation of experimental data [14], experimental results for cementite particles in a ferrite matrix [45,46], and results obtained from simulations with a Monte Carlo Potts model [19] and with a phase-field model [26].

The fits corresponding to each measure are shown in Fig. 8, computed for each aspect ratio separately. Relation (16) has predictive value if the graphs for the three aspect ratios coincide. The three graphs in Fig. 8a are distinctly separated, with the $r_a = 1$ -graph on top and the $r_a = 3$ -graph at the bottom. The measure $m = l$ thus seems to be less appropriate. In Fig. 8b, the graphs lie surprisingly close to each other, even though the measure $m = s$ does not include information on the aspect ratio. In Fig. 8c, the graphs for $r_a = 1$ and $r_a = 2$ almost coincide, while the graph for $r_a = 3$ lies a little lower. As mentioned in the previous subsection, distributions of particles with higher aspect ratio therefore seem to have a stronger pinning effect for the same volume fraction and particle volume. Note that the simulation

results of the parameter combination $f_V = 5\%$ and $r_a = 1$ were excluded from the fitting calculations, since only one simulation run with this parameter combination contained a sufficient number of grains at equilibrium.

Table 2 shows the estimated values for the parameters K and b obtained by fitting relation (16) to the simulation data for the three different aspect ratios r_a and the three different measures m . There is a very good correspondence of the data for $r_a = 1$ with the simulation results of [19], as illustrated in Fig. 7. As described in Section 4.3, it was found that the number of particles at multiple junctions increases with increasing volume fraction and aspect ratio (see Figs. 5 and 6). Still, the values obtained for the parameter b agree very well with those obtained in [11,13], where $b = 0.92$ and $b = 0.93$, respectively, were theoretically predicted assuming that the main contribution to the pinning effect comes from particles interacting with grain boundaries. An exponent slightly smaller than 1 is sometimes explained by a decrease in flexibility of the grain boundary with increasing volume fraction of the particles [13,45]. Irrespective of the exact explanation for the deviation from 1, the value for b seems to be independent of the aspect ratio of the particles. Refitting of the data for b fixed, namely $b = 0.93$, gives values for K as listed in Table 3. The values of K obtained for $m = l$ differ more strongly than those obtained for $m = s$ and $m = (ls^2)^{\frac{1}{3}}$. However, for all three measures m , it seems to be more appropriate to have a prefactor K that is a function of the particle aspect ratio. Such a relation is derived in the next section.

5.2. Analytical derivation

The simulations show that most particles interacting with a grain boundary are oriented with their major axis parallel with the grain boundary. Furthermore, the finding that $b = 0.93$ indicates that the assumption of random intersections between grain boundaries and particles is reasonable. Therefore, as a first

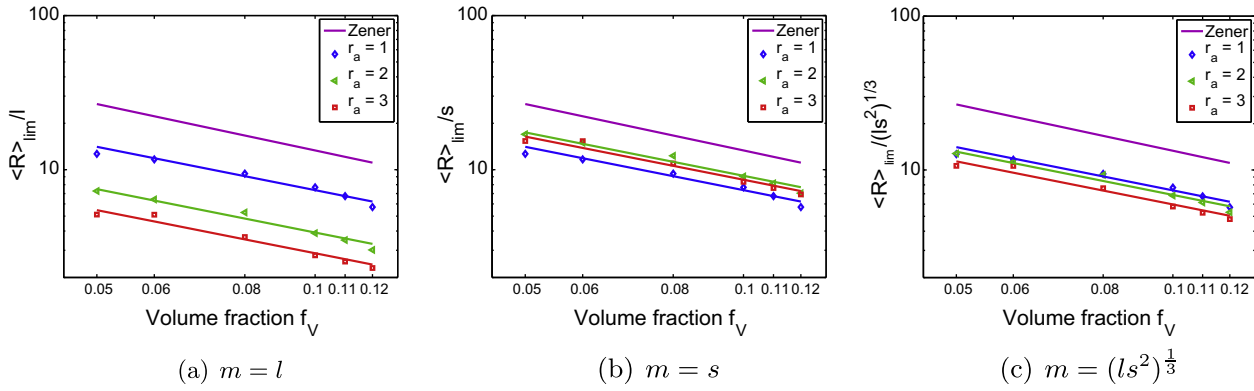


Fig. 8. Fits of relation (16) to the limiting mean grain radius divided by (a) $m = l$, (b) $m = s$ and (c) $m = (ls^2)^{1/3}$, for all tested volume fractions f_v and for the three aspect ratios r_a separately. The Zener relation (16) only has predictive value if the graphs coincide for the different aspect ratios. The measure $m = l$ is not appropriate, since the graphs are clearly separated. For $m = s$ and $m = (ls^2)^{1/3}$, the three graphs are close to each other.

Table 2

Estimated values for the parameter set (K, b) in Zener relation (16) for three different aspect ratios r_a and three different measures m of the second-phase particles.

m	l	s	$(ls^2)^{1/3}$
$r_a = 1$	(0.8593, 0.9333)	(0.8593, 0.9333)	(0.8593, 0.9333)
$r_a = 2$	(0.4557, 0.9339)	(1.0633, 0.9339)	(0.8017, 0.9339)
$r_a = 3$	(0.3377, 0.9295)	(1.0131, 0.9295)	(0.7024, 0.9295)

Table 3

Estimated values for the parameter K in Zener relation (16) for a fixed parameter $b = 0.93$, for three different aspect ratios r_a and three different measures m of the second-phase particles.

m	l	s	$(ls^2)^{1/3}$
$r_a = 1$	0.8664	0.8664	0.8664
$r_a = 2$	0.4606	1.0746	0.8102
$r_a = 3$	0.3372	1.0116	0.7015

approximation, we repeat the Zener–Smith analysis [11,14], but adapted for spheroid particles with their major axis parallel with the grain boundary.

The pinning force of a spheroid particle interacting with a grain boundary and oriented with its major axis parallel with the boundary axis is described by Eq. (2) [34]. The maximal pinning force of a spherical particle with equal volume is given by

$$F_Z^S = \pi r^* \sigma_{gb} = \pi (ls^2)^{1/3} \sigma_{gb}, \quad (17)$$

where the radius r^* is computed as the geometrical mean of the radii of the spheroid particle. The maximal pinning force of the spheroid particle is therefore

$$F_Z^{\max} = (ls^2)^{1/3} \sigma_{gb} \frac{1 + 2.14 r_a}{r_a^{1/3}} = s \sigma_{gb} (1 + 2.14 r_a). \quad (18)$$

Following the original derivation of Zener [44], we assume that all grain boundaries are flat and that all particles are uniformly distributed in space. Furthermore, all particles interacting with boundaries are assumed to be oriented with their major axis parallel with the boundary and exert their maximal force F_Z^{\max} . The number of particles interacting with a grain boundary per unit volume is accordingly

$$n_V = \frac{f_V}{\frac{4}{3} \pi ls^2} \times 2s = \frac{6f_V}{4\pi ls}, \quad (19)$$

assuming that all particles located within a distance of s on either side of the boundary interact with the boundary. The total pinning

force exerted per unit of grain boundary area by the distribution of particles thus equals

$$F_Z^{\text{tot}} = F_Z^{\max} \times n_V = (1 + 2.14 r_a) \frac{6f_V \sigma_{gb}}{4\pi l}. \quad (20)$$

The driving force F_D for grain boundary movement is given by

$$F_D = \frac{2\alpha \sigma_{gb}}{R}, \quad (21)$$

with α a geometrical constant [31]. Grain growth will stop when the driving force for grain boundary movement is equalled by the total pinning force F_Z^{tot} or when

$$\frac{2\alpha \sigma_{gb}}{\langle R \rangle_{\text{lim}}} = (1 + 2.14 r_a) \frac{6f_V \sigma_{gb}}{4\pi l}. \quad (22)$$

This equation yields a Zener type relation of the form

$$\frac{\langle R \rangle_{\text{lim}}}{l} = K \frac{1}{1 + 2.14 r_a f_V}, \quad (23)$$

with K a constant coefficient. Generalising this relation gives

$$\frac{\langle R \rangle_{\text{lim}}}{l} = K \frac{1}{1 + ar_a f_V^b}, \quad (24)$$

with K , a and b parameters that can be obtained by fitting the relation to simulation data. If the short axis s is used as a measure for the particle size, the generalised Zener relation for spheroid particles becomes

$$\frac{\langle R \rangle_{\text{lim}}}{s} = K \frac{r_a}{1 + ar_a f_V^b}, \quad (25)$$

since $r_a = l/s$. Similarly, if the geometric mean $(ls^2)^{1/3}$ of the three axis radii is used as a measure for the particle size, the generalised Zener relation becomes

$$\frac{\langle R \rangle_{\text{lim}}}{(ls^2)^{1/3}} = K \frac{(r_a)^{2/3}}{1 + ar_a f_V^b}. \quad (26)$$

Fig. 9 shows a plots of prefactor $1/(1 + ar_a)$ in relation (24), of prefactor $r_a/(1 + ar_a)$ in relation (25) and of prefactor $(r_a)^{2/3}/(1 + ar_a)$ in relation (26) respectively, for $a = 2.14$. Since the first and the third prefactor tend to zero for high aspect ratios, whereas the prefactor of relation (25) tends to a constant value $1/a$, it is most appropriate to use s as a measure for the particle size in the generalised Zener relation. Fig. 9 also shows that variations in the prefactors decrease for increasing aspect ratio, but are

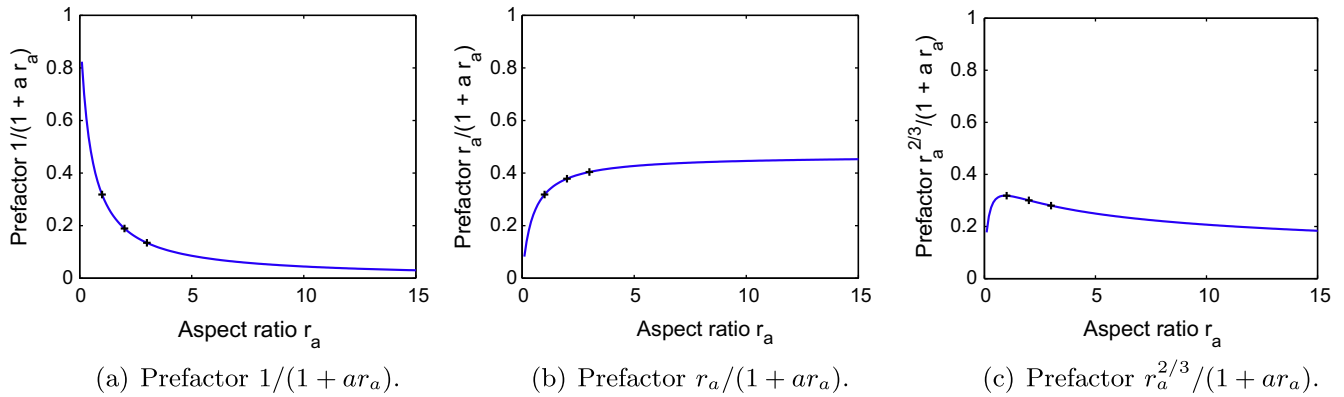


Fig. 9. Plots of the prefactors of (a) relation (24), (b) relation (25) and (c) relation (26) as a function of the aspect ratio r_a , for $a = 2.14$. All plots show that variations with r_a decrease with increasing aspect ratio and are relatively small for $r_a > 2$. The prefactor values for $r_a = 1, 2$, and 3 are indicated.

relatively large for $r_a \leq 2$. This explains why the graphs in Fig. 8 do not coincide. From relation (25), one may however expect that all curves for $\langle R \rangle_{\text{lim}}/s$ in Fig. 8b will coincide for higher aspect ratios.

Fitting relation (25) to all the simulation data at once, including the data obtained from the simulation run for parameter combination $f_v = 5\%$ and $r_a = 1$, yields the parameter values $(K, b, a) = (3.2774 \pm 2.1646, 0.9040 \pm 0.1392, 2.5492 \pm 1.6789)$. The 95% confidence interval is much smaller for the parameter b than for the other two parameters. Also, the value found for the parameter a is of the same order as the theoretical value 2.14. We stress however that more data points, considering higher aspect ratios and different orientation distributions of the particles, are required for a more accurate fit.

6. Conclusions

A common technique to control the grain size of a material is by the addition of impurities, which leads to the formation of second-phase particles. These particles inhibit grain boundary movement during grain growth. Despite long-standing research, there is still a large discrepancy between the final grain sizes predicted by theory and simulation and those measured for real materials. To gain more insight in this pinning phenomenon, the effect of particles with a spheroid shape on grain growth is studied in this work using three-dimensional phase-field simulations.

In order to simulate grain growth in the presence of second-phase particles with constant properties, the phase-field model of [35], extended in [24], is employed. The studied particles are spheroid and characterised by their aspect ratio r_a , which is the ratio between the long axis radius and the short axis radius of a particle. As phase-field simulations for grain growth are computationally very intensive, a parallel version of the bounding box algorithm [28] is implemented to perform the simulations in an efficient and fast way. Simulations are performed for different volume fractions, ranging from $f_v = 5\%$ to 12% , and three different aspect ratios: $r_a = 1, 2$ and 3 . For every parameter combination, the results are averaged over three simulation runs.

The pinning effect of a particle distribution is found to be stronger for increasing volume fraction, and for increasing aspect ratio. Similarly, the total fraction of particles present at boundaries increases with volume fraction and with aspect ratio, which is mostly due to an increase of the number of particles located at triple, quadruple or higher order junctions. The grain boundaries have the tendency to align themselves with the longest axis of the particles with $r_a = 3$. For aspect ratio $r_a = 2$, the extra amount of grain boundary (or curvature) that has to be created in the neighbourhood of a particle when the boundary reorients with

the long axis of the particle, seems to be too large compared to the amount of grain boundary removed by the particle after reorientation. Particles with $r_a = 3$ thus have a significant influence on the microstructural topology, especially at higher volume fractions. Nevertheless, the effect is still too small to fully explain the large difference between the final grain sizes obtained in simulations and those obtained experimentally.

In spite of the increasing number of particles located at boundary junctions, for all simulated aspect ratios, a volume fraction dependence of the limiting mean grain size of $1/f_v^{0.93}$ is obtained, which follows the theoretical predictions of [11,13] where a uniform distribution of spherical particles is assumed. Moreover, based on the simulation results, a generalised Zener type relation of the form

$$\frac{\langle R \rangle_{\text{lim}}}{s} = K \frac{r_a}{1 + ar_a} \frac{1}{f_v^b} \quad (27)$$

is proposed. More experimental and computational results are however required to describe the pinning effect of spheroid particles more accurately. For further research, it would be interesting, for example, to study the effect for a large range of aspect ratios and different orientation distributions of the particles.

Acknowledgements

Nele Moelans is Post-doctoral Fellow of the Research Foundation – Flanders (FWO).

The simulations were performed on the computer cluster of the HPC Computing Initiative, funded by the K.U.Leuven Research Council.

References

- [1] M. Chapa, B. Fernández, S.F. Medina, V. López, *ISIJ Int.* 42 (11) (2002) 1288–1296.
- [2] H. Ohta, R. Inoue, H. Suito, *ISIJ Int.* 48 (3) (2008) 294–300.
- [3] K. Song, M. Aindow, *Mater. Sci. Eng. A* 479 (1–2) (2008) 365–372.
- [4] A. Gangulee, F.M. D'Heurle, *Thin Solid Films* 16 (2) (1973) 227–236.
- [5] H.P. Longworth, C.V. Thompson, *J. Appl. Phys.* 69 (7) (1991) 3929–3940.
- [6] B.D. Knowlton, J.J. Clement, C.V. Thompson, *J. Appl. Phys.* 81 (9) (1997) 6073–6080.
- [7] G.D. Hibbard, J.L. McCrea, G. Palumbo, K.T. Aust, U. Erb, *Scripta Mater.* 47 (2) (2002) 83–87.
- [8] E. Ma, *JOM* 58 (4) (2006) 49–53.
- [9] C.C. Koch, R.O. Scattergood, K.A. Darling, J.E. Semones, *J. Mater. Sci.* 43 (23–24) (2008) 7264–7272.
- [10] B. Cherukuri, R. Srinivasan, S. Tamirisakandala, D.B. Miracle, *Scripta Mater.* 60 (7) (2009) 496–499.
- [11] E. Nes, N. Ryum, O. Hunderi, *Acta Metall.* 33 (1) (1985) 11–22.
- [12] R.D. Doherty, D.J. Srolovitz, A.D. Rollett, M.P. Anderson, *Scripta Metall.* 21 (1987) 675–679.
- [13] M. Hillert, *Acta Metall.* 36 (12) (1988) 3177–3181.

- [14] P.A. Manohar, M. Ferry, T. Chandra, *ISIJ Int.* 38 (9) (1998) 913–924.
- [15] W.-B. Li, K.E. Easterling, *Acta Metall. Mater.* 38 (6) (1990) 1045–1052.
- [16] S.P. Ringer, W.B. Li, K.E. Easterling, *Acta Metall.* 37 (3) (1989) 831–841.
- [17] J. Gao, R.G. Thompson, B.R. Patterson, *Acta Mater.* 45 (9) (1997) 3653–3658.
- [18] M. Soucail, R. Messina, A. Cosnuau, L.P. Kubin, *Mater. Sci. Eng. A* 271 (1–2) (1999) 1–7.
- [19] M. Miodownik, E.A. Holm, G.N. Hassold, *Scripta Mater.* 42 (12) (2000) 1173–1177.
- [20] S.P. Riege, C.V. Thompson, H.J. Frost, *Acta Mater.* 47 (6) (1999) 1879–1887.
- [21] D. Weygand, Y. Bréchet, J. Lépinoux, *Mater. Sci. Eng. A* 292 (1) (2000) 34–39.
- [22] G. Couturier, R. Doherty, C. Maurice, R. Fortunier, *Acta Mater.* 53 (4) (2005) 977–989.
- [23] D. Fan, L.-Q. Chen, S.-P.P. Chen, *J. Am. Ceram. Soc.* 81 (1998) 526–532.
- [24] N. Moelans, B. Blanpain, P. Wollants, *Acta Mater.* 53 (2005) 1771–1781.
- [25] N. Moelans, B. Blanpain, P. Wollants, *Acta Mater.* 54 (2006) 1175–1184.
- [26] Y. Suwa, Y. Saito, H. Onodera, *Scripta Mater.* 55 (2006) 407–410.
- [27] N. Moelans, B. Blanpain, P. Wollants, *Acta Mater.* 55 (2007) 2173–2182.
- [28] L. Vanherpe, N. Moelans, B. Blanpain, S. Vandewalle, *Phys. Rev. E* 76 (2007) 056702.
- [29] K. Chang, W. Feng, L.-Q. Chen, *Acta Mater.* 57 (17) (2009) 5229–5236.
- [30] M. Apel, B. Böttger, J. Rudnizki, P. Schaffnit, I. Steinbach, *ISIJ Int.* 49 (7) (2009) 1024–1029.
- [31] F.J. Humphreys, M. Hatherly, *Recrystallization and Related Annealing Phenomena*, Elsevier, Oxford, 1995.
- [32] N. Sun, B.R. Patterson, J.P. Suni, H. Weiland, L.F. Allard, *Acta Mater.* 54 (2006) 4091–4099.
- [33] A. Harun, E.A. Holm, M.P. Clode, M.A. Miodownik, *Acta Mater.* 54 (2006) 3261–3273.
- [34] N. Ryum, O. Hunderi, E. Nes, *Scripta Mater.* 17 (1983) 1281–1283.
- [35] L.-Q. Chen, W. Yang, *Phys. Rev. B* 50 (21) (1994) 15752–15756.
- [36] D. Fan, L.-Q. Chen, *Acta Mater.* 45 (1997) 611–622.
- [37] E. Anselmino, *Microstructural effects on grain boundary motion in Al–Mn alloys*, Ph.D. thesis, TUDelft, 2007.
- [38] L.-Q. Chen, J. Shen, *Comput. Phys. Commun.* 108 (1998) 148–158.
- [39] J. Gruber, N. Ma, Y. Wang, A.D. Rollett, G.S. Rohrer, *Model. Simul. Mater. Sci.* 14 (14) (2006) 1189–1195.
- [40] S. Vedantam, B.S.V. Patnaik, *Phys. Rev. E* 73 (2006) 016703.
- [41] S.G. Kim, D.I. Kim, W.T. Kim, Y.B. Park, *Phys. Rev. E* 74 (6) (2006) 061605.
- [42] L. Vanherpe, N. Moelans, B. Blanpain, S. Vandewalle, *Proc. Appl. Math. Mech.* 7 (2007) 2020001–2020002.
- [43] Y. Bréchet, M. Militzer, *Scripta Mater.* 52 (2005) 1299–1303.
- [44] C. Smith, *Trans. Metall. Soc. AIME* 175 (1948) 15.
- [45] P. Hellman, M. Hillert, *Scand. J. Metall.* 4 (5) (1975) 211–219.
- [46] L. Anand, J. Gurland, *Metall. Trans. A* 6 (4) (1975) 928–931.